batteries

MDPI

Article

Hierarchical $CaMn_2O_4$/C Network Framework toward Aqueous Zn Ion Hybrid Capacitors as Competitive Cathodes

Lifen Ding [1], Qingchao Gao [2,3,*] and Changzhou Yuan [3]

[1] School of Mechanical and Electronic Control Engineering, Beijing Jiaotong University, Beijing 100044, China; lfding@bjtu.edu.cn
[2] Shenzhen Major Industry Investment Group & Tankeblue Semiconductor Co., Ltd., Shenzhen 518108, China
[3] School of Materials Science & Engineering, University of Jinan, Jinan 250022, China; mse_yuancz@ujn.edu.cn
* Correspondence: agaoqc_me@163.com

Abstract: Manganese-based materials have received more attention as cathodes for aqueous zinc ion hybrid capacitors (AZIHCs) due to their advantages such as abundant reserves, low cost, and large theoretical capacity. However, manganese-based materials have the disadvantage of poor electrical conductivity. Herein, a solid-phase method was used to synthesize a hierarchical carbon-coated calcium manganate ($CaMn_2O_4$/C) network framework as the cathode for AZIHCs. Thanks to the unique structural/componential merits including conductive carbon coating and hierarchical porous architecture, the achieved $CaMn_2O_4$/C cathode shows an exceptionally long life of close to 5000 cycles at 2.0 A g^{-1}, with a reversible specific capacity of 195.6 mAh g^{-1}. The assembled $CaMn_2O_4$/C-based AZIHCs also display excellent cycling stability with a capacity retention rate of 84.9% after 8000 cycles at 1.0 A g^{-1}, and an energy density of 21.3 Wh kg^{-1} at an output power density of 180.0 W kg^{-1}.

Keywords: $CaMn_2O_4$/C; hierarchical porous; network framework; cathodes; aqueous zinc ion hybrid capacitors

check for updates

Citation: Ding, L.; Gao, Q.; Yuan, C. Hierarchical $CaMn_2O_4$/C Network Framework toward Aqueous Zn Ion Hybrid Capacitors as Competitive Cathodes. *Batteries* **2023**, *9*, 586. https://doi.org/10.3390/batteries9120586

Academic Editor: Pascal Venet

Received: 31 October 2023
Revised: 27 November 2023
Accepted: 28 November 2023
Published: 12 December 2023

1. Introduction

It is well known that non-renewable chemical energy sources such as coal, natural gas, and oil are decreasing, and the world is facing an energy crisis with rapid economic development. Ionic hybrid capacitors (IHCs) have both the higher power density of supercapacitors together with the higher energy density of secondary batteries, which is a promising energy storage device. The most mature research is on alkali ionic hybrid capacitors (AIHCs), and some of the research has been put into commercial use [1–3]. However, most AIHCs use organic electrolytes, which are not only costly but also highly flammable during use. Aqueous zinc ionic hybrid capacitors (AZIHCs) use water as a solvent, which not only saves cost but also reduces the combustion of the electrolyte [4–10]. In addition, AIHCs are manufactured in a more restrictive environment, whereas AZIHCs are manufactured in a milder environment. AZIHCs have great potential to become large-scale commercially available energy storage devices [11,12].

The main cathode materials for AZIHCs are vanadium-based oxides and manganese-based oxides. In recent years, researchers have studied vanadium-based oxides as electrode materials for AZIHCs. Ma et al. synthesized rod-shaped V_2O_5 as the cathode electrode material for AZIHCs [13], and AC was used as the anode electrode for assembling AZIHCs. By optimizing the mass ratio of the anode together with the cathode, the specific capacity of AZIHCs at 0.1 A g^{-1} is 57.4 mAh g^{-1}, and the maximum energy density was 34.6 Wh kg^{-1}. In addition, manganese-based oxides have received more attention due to their advantages of abundant reserves, low cost, multivalency, and high theoretical capacity [14–16]. However, manganese-based materials have the disadvantage of poor electrical conductivity as electrode materials, which leads to the poor rate performance and cycling performance of such materials [17–20]. Zeng et al. used ultrasonic treatment to prepare MnO_2-CNTs

composite electrodes [21]. The MnO_2-CNTs electrode had a high specific capacitance of 254.1 mAh g^{-1} (0.256 A g^{-1}). Gao et al. synthesize ZMO nanoparticles on heterostructures of carbon nanotubes for stable Zn^{2+} storage [22]. Highly conductive CNTs and smaller ZMO can promote fast electron transport and make the ZMO/CNTs composites have high electrical conductivity. The results showed that the prepared ZMO/CNTs materials exhibited excellent cycling stability with an initial specific capacity of 220.3 mAh g^{-1} at 0.1 A g^{-1}.

In this work, hierarchical carbon-coated calcium manganate ($CaMn_2O_4$/C) network framework was synthesized by a simple yet mass-producible solid-phase method using polyvinyl pyrrolidone (PVP) as the carbon source, $Ca(NO_3)_2{\cdot}4H_2O$ together with $Mn(NO_3)_2{\cdot}4H_2O$ as the calcium and manganese sources, respectively. The introduction of C into $CaMn_2O_4$/C increased its electrical conductivity. As a result, the $CaMn_2O_4$/C cathode materials exhibit an exceptionally long lifetime of nearly 5000 cycles at 2.0 A g^{-1} with a reversible specific capacity of 195.6 mAh g^{-1}. The assembled AZIHCs were obtained by using porous carbon (PC) as the anode and $CaMn_2O_4$/C as the cathode as well as a mixed aqueous solution (0.2 M $MnSO_4$ and 2.0 M $ZnSO_4$) as the electrolyte. The constructed PC//$CaMn_2O_4$/C AZIHCs achieve an energy density of 21.3 Wh kg^{-1} at a power density of 180.0 W kg^{-1}, along with modest device leakage current and self-discharge capability, and favorable cycling stability with 84.9% capacity retention after 8000 cycles at 1.0 A g^{-1}.

2. Experimental Sections

2.1. Chemicals

The chemical reagents including $Mn(NO_3)_2{\cdot}4H_2O$, $Ca(NO_3)_2{\cdot}4H_2O$, N-methyl-2-pyrrolidinone (NMP), $ZnSO_4$, $MnSO_4$, and polyvinylpyrrolidone (PVP, K30) are of analytic grade, and from Sinopharm Chemical Reagent Co., Ltd. (Shanghai, China). The chemical reagents are directly used as received without further treatment.

2.2. Materials Synthesis

Synthesize of $CaMn_2O_4$/C: 0.4 g of PVP, 0.258 g of $Ca(NO_3)_2{\cdot}4H_2O$ and 0.752 g of $Mn(NO_3)_2{\cdot}4H_2O$ were well prepared in a mortar, ground thoroughly for 30 min. The milled powder was placed in a muffle furnace, heated up to 750 °C held for 3 h at a rate of 5 °C min^{-1}. The resulting sample was named $CaMn_2O_4$/C.

Synthesis of PC materials: The PC material was fabricated according to the previous report [23]. $Zn(NO_3)_2{\cdot}6H_2O$ and PVP(K30) were dissolved in sufficient distilled water in the mass ratio of 1.5:1 and stirred for 30 min. Then, the resulting solution was placed in an oven (at 90 °C) and dried completely. The powder was annealed at 800 °C for 1 h (atmosphere: N_2, rate: 5 °C min^{-1}). The annealed sample and KOH were dissolved in deionized water in the ratio of 1:3 by mass and stirred for 30 min. The resulting solution was dried (at 90 °C) completely. The dried mixture is then activated at 800 °C for 3 h (atmosphere: N_2, rate: 5 °C min^{-1}). The excess KOH in the product is neutralized by aqueous hydrochloric acid. The product was washed with plenty of deionized water and dried at 60 °C for 12 h (in an oven). The sample was named PC.

2.3. Material Characterization

Phase characterization of products was carried out using X-ray diffraction (XRD, Rigaku Ultima IV powder X-ray diffractometer with Cu Ka radiation). The chemical compositions were tested by X-ray photoelectron spectroscopy (XPS, The model number is VG Multilab 2000 and the origin is England). Raman spectra (HR Evolution, Japanese) were collected using 532 nm excitation. The microstructures and morphologies of samples were characterized using transmission electron microscopy (TEM), field-emission scanning electron microscopy (FESEM, JEOL-6300F), and high-resolution TEM (HRTEM, the model is JEM-2100 and the manufacturer is Nippon Electronics Co., Ltd., Mumbai, India).

2.4. Electrochemical Measurements

Preparation of $CaMn_2O_4$/C cathode: Briefly, a mixture of poly(vinylidene fluoride) (PVDF): $CaMn_2O_4$/C: acetylene black was added to the mortar in the mass ratio of 1:7:2, and a reasonable amount of NMP was added dropwise, and the paste was ground for 40 min to form a homogeneous paste. The slurry was evenly coated on a 12 mm diameter carbon paper, placed in an oven, and dried overnight at 110 °C. The amount of the $CaMn_2O_4$/C on the carbon paper was about 1.5 mg.

Preparation of PC anode: Typically, a mixture of PVDF:acetylene black:PC was added to the mortar in a mass ratio of 1:2:7. A reasonable amount of NMP was added dropwise and the paste was ground for half an hour to form a homogeneous slurry. The slurry was uniformly coated on a stainless-steel mesh of 12 mm in diameter and then placed in an oven for drying overnight at 60 °C. The mass loading of PC on the stainless-steel mesh was around 1.0 mg.

Glass fiber (Whatman GF/D) was used for the diaphragm, zinc foil was used as the reference electrode, and a mixture of 0.2 M $MnSO_4$ and 2.0 M $ZnSO_4$ in aqueous solution was used for the electrolyte. The CR2016 button half-cell was assembled to study the electrochemical performance of $CaMn_2O_4$/C. The voltage range was 0.4–1.9 V (vs. Zn/Zn^{2+}).

$CaMn_2O_4$/C was used as the cathode along with PC as the anode to assemble the AZIHCs. The separator and electrolyte were kept the same as those for the electrochemical evaluation of $CaMn_2O_4$/C, as mentioned above. The devices were tested over a voltage range of 0–1.8 V. Galvanostatic intermittent titration technique (GITT) and typical charge/discharge tests were conducted on an 8-channel Land Test System (CT2001A). Cyclic voltammetry (CV) was performed on the electrochemical workstation (IviumStat. h, Eindhoven, The Netherlands) at 25 °C.

3. Results and Discussion

3.1. Synthesis and Structural Analysis

The microstructures of the as-obtained $CaMn_2O_4$/C are characterized by FESEM. As illustrated in Figure 1a, the hierarchical porous network framework is evident for the $CaMn_2O_4$/C, which is constructed with nano-building blocks of about 0.2 μm in size (Figure 1b,c). The co-existence of Ca, Mn, and O species can be visualized based on the elemental mapping images (Figure 1d–f), moreover, the C mapping image authenticates the uniform distribution in the $CaMn_2O_4$/C composite framework (Figure 1g). In addition, by EDS spectroscopy data, the $CaMn_2O_4$/C composites had a C relative atomic ratio is about 8.29 at.% (Figure S1). As shown in Figure S2, we performed a Raman spectroscopic evaluation of $CaMn_2O_4$/C. The G and D bands of carbon are located at 1607.2 cm^{-1} and 1333.9 cm^{-1}, respectively, indicating the presence of graphitic structures and defects/disturbances. The intensity ratio (i.e., I_D/I_G) of the D and G bands can be used to estimate the degree of graphitization, which is 1.35 for $CaMn_2O_4$/C.

The more detailed structure of $CaMn_2O_4$/C was characterized as well by TEM and HRTEM techniques, as shown in Figure 2a,b. Clearly, a uniform carbon layer of about 3.53 nm in thickness is located upon the surface of the well-crystalline $CaMn_2O_4$, and the well-defined lattice fringes with a spacing of 0.300 nm, which corresponds to the (320) lattice plane of $CaMn_2O_4$, is apparent.

The crystal structures of the resulting $CaMn_2O_4$/C were checked by XRD. As illustrated in Figure 3, typical XRD peaks here match well with the standard data of the $CaMn_2O_4$ (JCPDS PDF# 76-0516). In specific, the distinct diffraction peaks at 2θ = 18.3, 31.0, 32.9, 35.0, 39.2, 40.3, 40.5, and 43.5° are related to (200), (111), (320), (211), (031), (131), (240) and (231) planes, respectively [24,25]. Moreover, no other discernable reflections are found for the potential impurities, suggesting that the $CaMn_2O_4$/C is successfully prepared by such a facile synthetic method.

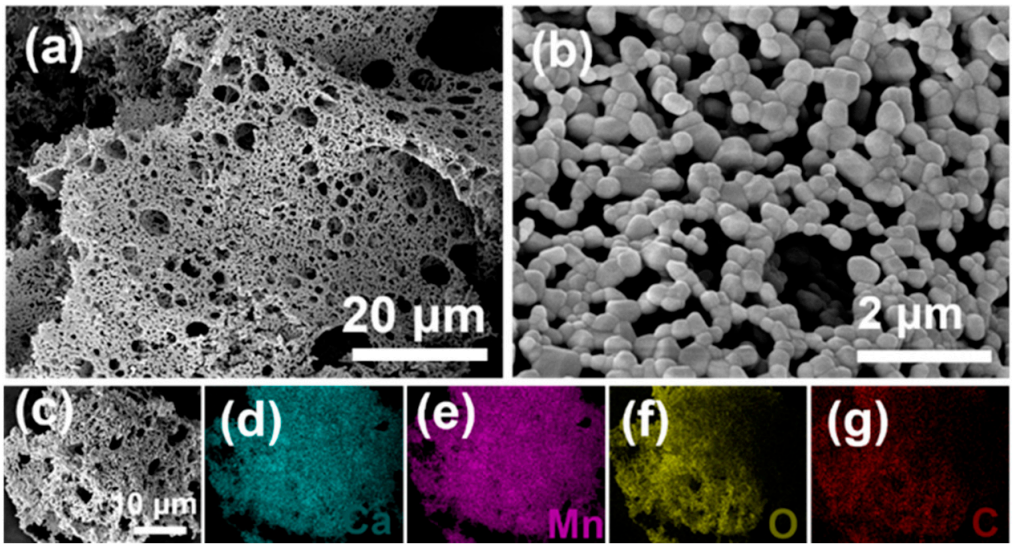

Figure 1. (**a**–**c**) FESEM images, and corresponding elemental ((**d**) Ca; (**e**) Mn; (**f**) O and (**g**) C) mapping images of $CaMn_2O_4$/C.

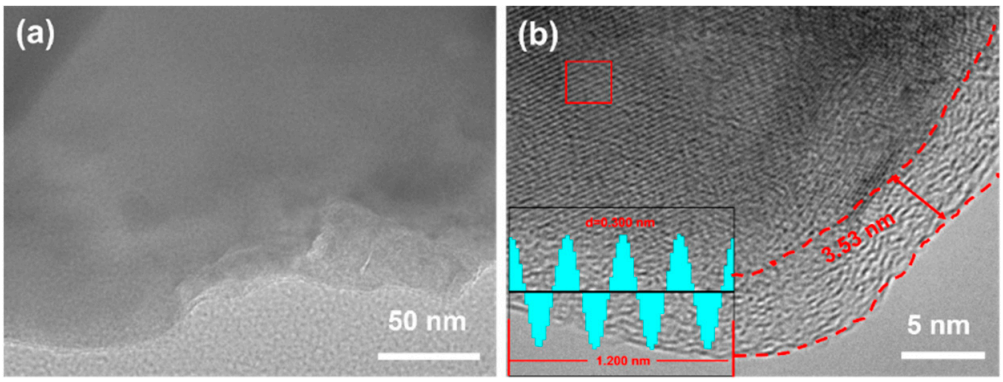

Figure 2. (**a**) TEM and (**b**) HRTEM images of $CaMn_2O_4$/C. The inset for the intensity profile for the measured interlayer spacing.

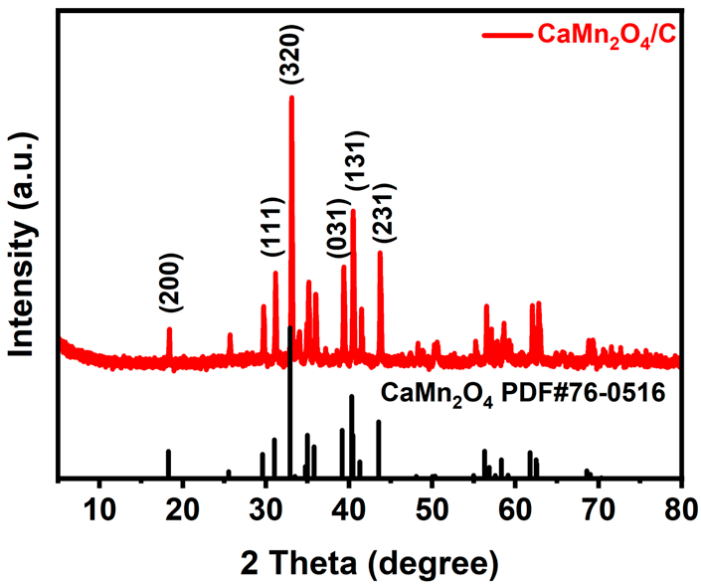

Figure 3. XRD pattern of $CaMn_2O_4$/C.

XPS determinations of $CaMn_2O_4/C$ were performed to enable further analysis of the chemical state of the surface elements. As illustrated in Figure 4a, the characteristic peaks of C 1s, Mn 2p, O 1s, and Ca 2p can be observed. Figure 4b shows the XPS spectrum of Mn 2p, and the characteristic peaks at 641.8 and 653.0 eV correspond to Mn $2p_{3/2}$ and Mn $2p_{1/2}$ [25,26]. As illustrated in Figure 4c, the O 1s spectrum of $CaMn_2O_4/C$ can be divided into two peaks at 529.2 (metal-oxygen bond) and 531.2 (O-H) eV [25,26]. The Ca spectrum of $CaMn_2O_4/C$, as presented in Figure 4d, is fitted as two peaks corresponding to Ca $2p_{3/2}$ (350.3 eV) and Ca $2p_{3/2}$ (346.8 eV), respectively [27]. The C 1s spectrum (Figure 4e), can be decomposed into three peaks at 284.5, 285.8, and 285.0 eV, corresponding to C-C, O-C=C, and C-O, respectively [26].

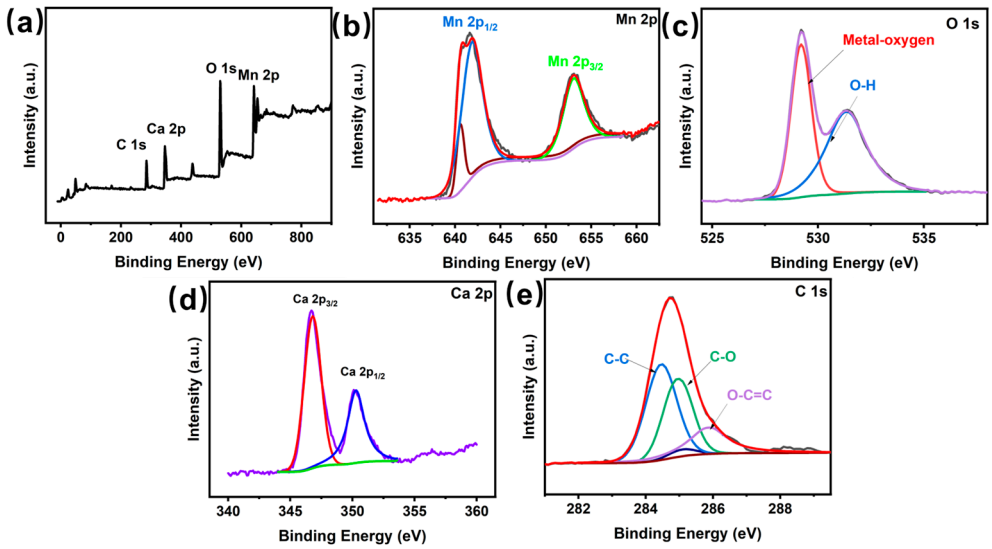

Figure 4. High-resolution core-level spectra of (**a**) XPS survey spectrum, (**b**) Mn 2p, (**c**) O 1s, (**d**) Ca 2p, and (**e**) C 1s, respectively, for the $CaMn_2O_4/C$ sample.

3.2. Electrochemical Evaluation of the $CaMn_2O_4$/C Cathode

As illustrated in Figure 5, the electrochemical performance of $CaMn_2O_4/C$ is collected. The initial three CV curves of $CaMn_2O_4/C$ are shown in Figure 5a. The CV curves for the initial cycle under a scanning rate of 0.1 mV s^{-1} are slightly different from the subsequent ones, which may be relevant to the progressive activation of the electrode in subsequent cycles. For the anodic scan of the second cycle, two peaks centered at 1.60 as well as 1.54 V appear and overlap in the CV curve, which corresponds to the progressive electrochemical extraction of Zn^{2+} [28]. In the cathodic scan, two distinct peaks were observed (around 1.38 as well as 1.23 V), which could be ascribed to the gradual embedding of Zn^{2+} [29]. The constant current charge/discharge plots of $CaMn_2O_4/C$ at 0.1 A g^{-1} are profiled in Figure 5b. $CaMn_2O_4/C$ displays a discharge-specific capacity of 248.1 mAh g^{-1} (at 0.1 A g^{-1}). The rate behaviors of the $CaMn_2O_4/C$ are summarized, as shown in Figure 5c. The $CaMn_2O_4/C$ cathode provides reversible specific capacities of 260.9, 242.3, 219.9, 198.3, 135.1, and 112.2 mAh g^{-1} at 0.4, 0.6, 0.8, 1.0, 2.0, and 3.0 A g^{-1}, respectively, equivalenting to a capacity retention of 43%. When the current density is again returned to 0.4 A g^{-1}, a reversible specific capacity as high as 275.0 mAh g^{-1} is remained by $CaMn_2O_4/C$ cathode. This excellent rate performance, as summarized in Figure 5d, is also comparable to many other cathode materials recently reported in the literature, such as $Ca_{0.28}MnO_2{\cdot}0.5\,H_2O$ [25], ZMO@$Ti_3C_2T_x$ [27], ZMO QD@C [30], ZMO [31], and K, Fe-ZMO [32]. More surprisingly, our fabricated $CaMn_2O_4/C$ cathode exhibits robust electrochemical stability with an exceptionally long lifetime of 5000 cycles at 2.0 A g^{-1} with a retained reversible capacity of 195.6 mAh g^{-1}, as illustrated in Figure 5e.

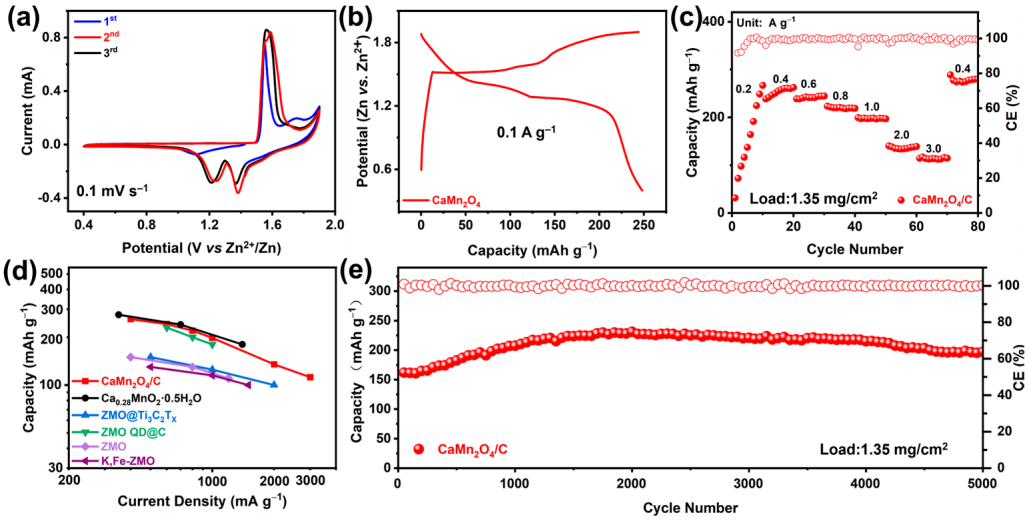

Figure 5. (**a**) CV curves and (**b**) the first charge/discharge plots (0.1 A g^{-1}), (**c**) rate behaviors, (**d**) comparison in rate capacities with other cathodes reported in the literature in recent years, and (**e**) long cycling performance (1.0 A g^{-1}) of the $CaMn_2O_4$/C cathode.

The GITT tests were utilized to investigate the diffusion coefficient (D_{Zn}) of Zn^{2+} during the charging/discharging processes of $CaMn_2O_4$/C (Figure S3). The GITT was performed after three charging and discharging cycles of the $CaMn_2O_4$/C half-cell. The GITT was carried out with the relaxation time of 30 min at 0.2 A g^{-1} and the charging and discharging time of 10 min. The D_{Zn} values of $CaMn_2O_4$/C are calculated according to the equation [20]:

$$D_{Zn} = \frac{4L^2}{\pi\tau}\left(\frac{m_b V_M}{M_B S}\right)^2\left(\frac{\Delta E_S}{\Delta E_t}\right)^2 \quad (1)$$

where m_b, V_M, and M_B represent the mass, molar volume of the active material, and molar mass, respectively. S corresponds to the surface area, τ corresponds to the relaxation time, ΔEs for the steady-state potential change of the current pulse, and ΔE_t for the iR drop after relaxation time. The D_{Zn} values of $CaMn_2O_4$/C were then calculated to be in the range of 10^{-12} and 10^{-10} cm^2 s^{-1} over the discharge-charge processes (Figure 6a,b). This is also consistent with its better cycling and multiplication properties [33].

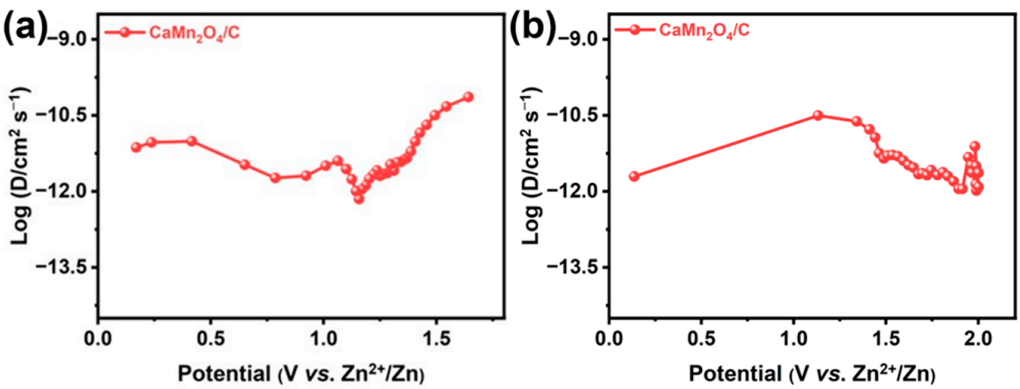

Figure 6. Specific D_{Zn} values over the (**a**) discharge and (**b**) charging processes of the $CaMn_2O_4$/C cathode.

In order to deeply analyze the storage kinetics of Zn^{2+}, CV measurements of $CaMn_2O_4$/C were carried out under different scanning rates of 0.2–1.0 mV s^{-1}. Two reduction peaks and one oxidation peak can be clearly observed (Figure 7a). The profile of the CV curves of $CaMn_2O_4$/C does not appear significantly with increasing scan rate, indicating that it has good reaction kinetics. The capacitance effect of the cathode is calculated from the relationship between the current (i) as well as the scan rate (v) by the equation: $i = av^b$

(b as well as a are constants). Generally, the value of b is equal to 0.5 for ion diffusion-controlled processes, and the case of $b = 1$ corresponds to the surface capacitance-controlled processes, and the value of b is greater than 0.5 but less than 1, which indicates a mixed mechanism. The b values of peak 1, peak 2, and peak 3 are 0.71, 0.73 and 0.72 (Figure 7b) [24], which indicates the pseudocapacitive contribution dominated Zn^{2+}-storage process for the $CaMn_2O_4/C$ composite cathode. Specific pseudocapacitive contribution of the cathode can be distinguished by the equation: $i = k_1v + k_2v^{1/2}$, where k_1v and $k_2v^{1/2}$ represent the one from the capacitive part and the current of the diffusion-controlled part. Figure 7c shows the capacity share contributed by the diffusion control process and the capacitive effect (red region) at 0.8 mV s^{-1}, highlighting a capacitive contribution as large as about 91.8% for the $CaMn_2O_4/C$ electrode. More strikingly, the capacitive contribution can be up to 92.7% when the sweep rate is up to 1.0 mV s^{-1} (Figure 7d). It is the remarkable capacitive contrition of the $CaMn_2O_4/C$ here that ensures its faster reaction kinetics toward efficient zinc storage [34,35].

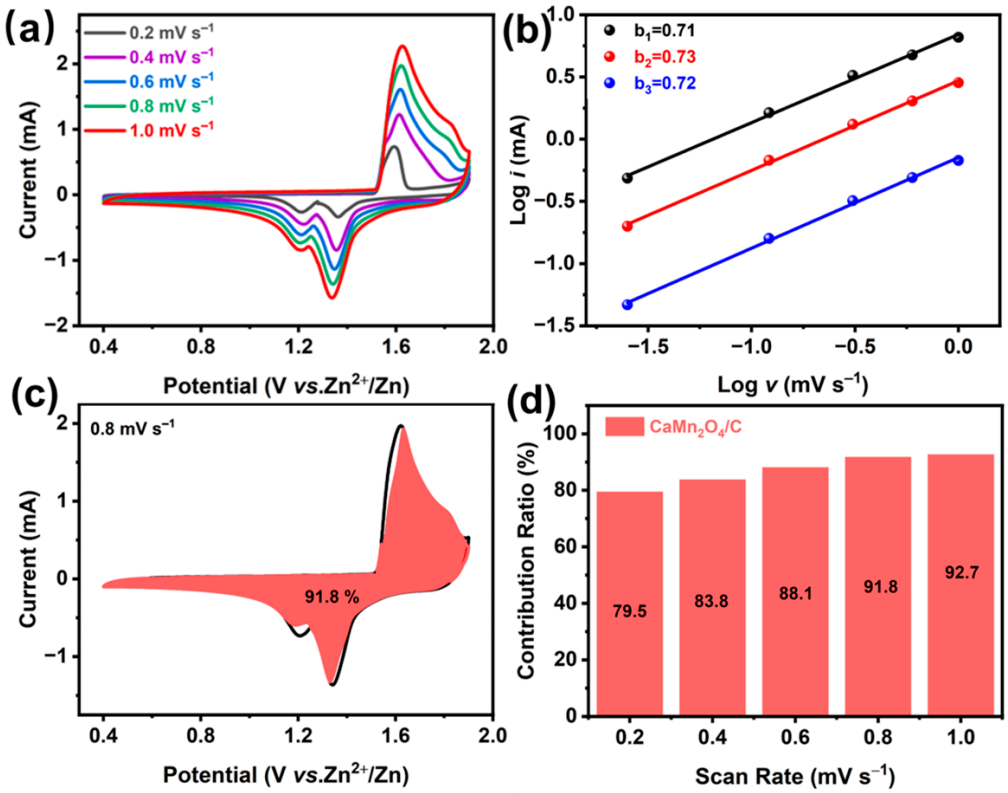

Figure 7. (**a**) CV curves, (**b**) corresponding logi vs. logv plots, (**c**) CV curves with the pseudocapacitive contribution (red region), and (**d**) diagram for the pseudocapacitive contributions at different scan rates for the $CaMn_2O_4/C$ cathode.

3.3. Electrochemical Properties of PC//$CaMn_2O_4$/C AZIHCs

The unique PC//$CaMn_2O_4/C$ AZIHCs were assembled with the $CaMn_2O_4/C$ as the cathode and the PC as the anode, as schematically illustrated in Figure 8a, and their electrochemical performance was comprehensively measured. Figure 8b shows the CV curves of AZIHCs at 5.0–40.0 mV s^{-1} (the voltage range: 0–1.8 V). The device CV curves at 5.0–40.0 mV s^{-1} are close to an ideal rectangular shape, showing the characteristic capacitive nature of the hybrid device. The profile of the CV curve does not appear to change with increasing scanning rate, indicating modest polarization of the AZIHCs occurring. Figure 8c exhibits the constant-current charge/discharge plots of the PC//$CaMn_2O_4/C$ AZIHCs. These curves are almost straight lines, showing the good capacitive characteristics of the AZIHCs. It is worth noting that the reversible capacitance of the cell can be as high as 80.0–17.8 F g^{-1} at 0.2–2.0 A g^{-1}. The device provides an energy density of 21.3 Wh kg^{-1}

at an output power density of 180.0 W kg^{-1}. When charged to 1.8 V at 0.1 A g^{-1}, the device leakage current was only 7 μA (Figure 8d) and the open-circuit voltage (after 20 h of static operation) dropped by 0.75 V, equivalenting to a voltage loss of only 41.6% (Figure 8e). As shown in Figure 8f, the AZIHCs exhibit excellent cycling stability with 84.9% capacity retention (at 1.0 A g^{-1}) after 8000 cycles, equivalenting to a capacitance degradation of 0.046% per cycle, indicative of superb electrochemical stability of our fabricated PC//$CaMn_2O_4$/C AZIHCs.

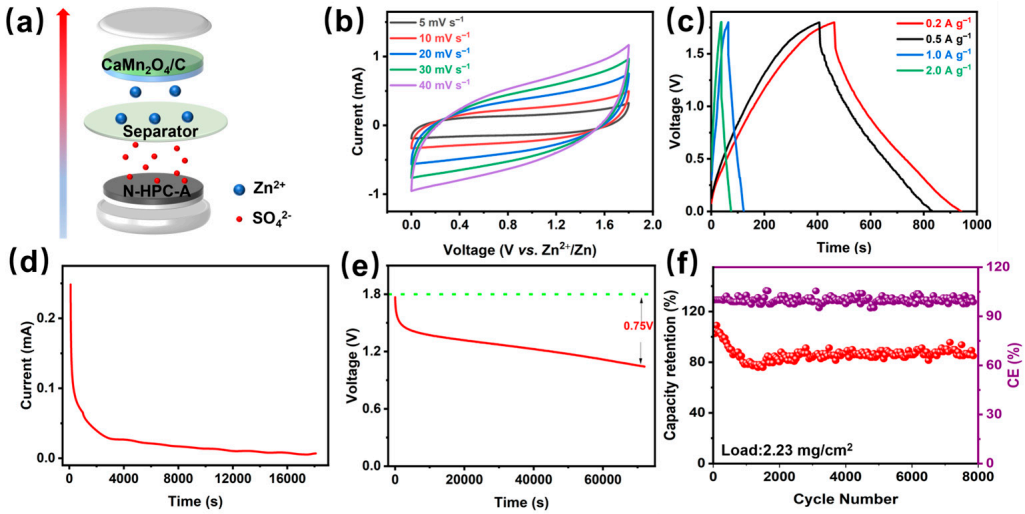

Figure 8. Electrochemical performance of N-HPC-A//$CaMn_2O_4$/C AZIHCs: (**a**) schematic diagram of device assembly, (**b**) CV curves, (**c**) constant current charge-discharge plots from 0.2 to 2.0 A g^{-1}, (**d**) leakage current diagram, (**e**) self-discharge diagram, and (**f**) cycling performance.

4. Conclusions

In summary, in our work, we explored a solid-phase synthesis avenue to smartly fabricate a hierarchical $CaMn_2O_4$/C network framework and utilize it as the competitive cathode for AZHICs. Benefiting from its unique structural/componential advantages, the $CaMn_2O_4$/C cathode was endowed with superb electrochemical stability and high-rate capacities. Typically, the cathode displayed an exceptionally long cycle life of nearly 5000 cycles at 2.0 A g^{-1}, with a reversible specific capacity of 195.6 mAh g^{-1}. Utilizing the PC as the anode, and $CaMn_2O_4$/C as the cathode, the assembled PC//$CaMn_2O_4$/C AZIHCs exhibited capacity retention of 84.9% (at 1.0 A g^{-1}) after 8000 cycles and a power density of 180.0 W kg^{-1} at an energy density of 21.3 Wh kg^{-1}. All the data here featured the good prospects of our prepared porous $CaMn_2O_4$/C network framework for practical applications.

Supplementary Materials: The following supporting information can be downloaded at: https://www.mdpi.com/article/10.3390/batteries9120586/s1, Figure S1: EDS spectrum of $CaMn_2O_4$/C and individual atoms percentage; Figure S2: Raman spectra of the $CaMn_2O_4$/C cathode; Figure S3: GITT curves overcharge and discharge processes of the $CaMn_2O_4$/C cathode.

Author Contributions: Conceptualization, L.D. and Q.G.; methodology, L.D.; software, L.D.; validation, L.D., Q.G. and C.Y.; formal analysis, L.D.; investigation, L.D.; resources, L.D.; data curation, Q.G. and C.Y.; writing—original draft preparation, L.D.; writing—review and editing, Q.G. and C.Y.; visualization, L.D.; supervision, Q.G.; project administration, Q.G. All authors have read and agreed to the published version of the manuscript.

Funding: This research received no external funding.

Data Availability Statement: Data are contained within the article or Supplementary Material.

Conflicts of Interest: The authors declare no conflict of interest.

References

1. Gopalakrishnan, A.; Sharma, C.S. High-performance dual carbon Li-ion hybrid capacitor constructed from N, S—Co-doped candle soot derived carbon nanoparticles anode and porous carbon cathode. *J. Energy Storage* **2022**, *55*, 105788. [CrossRef]
2. Wang, G.Y.; Wang, X.H.; Sun, J.F.; Zhang, Y.M.; Hou, L.R.; Yuan, C.Z. Porous carbon nanofibers derived from low-softening-point coal pitch towards all-carbon potassium ion hybrid capacitors. *Rare Met.* **2022**, *22*, 3706. [CrossRef]
3. Zhou, J.; Hu, H.Y.; Li, H.Q.; Chen, Z.P.; Yuan, C.Z.; He, X.J. Advanced carbon-based materials for Na, K, and Zn ion hybrid capacitors. *Rare Met.* **2023**, *42*, 719. [CrossRef]
4. Bommireddy, P.R.; Karnam, J.B.; Park, S. Ni-Co PBA-decorated CNTs as battery-type cathode materials for potassium-ion hybrid capacitors. *J. Energy Storage* **2023**, *62*, 106870. [CrossRef]
5. Rajkumar, P.; Thirumal, V.; Radhika, G.; Gnanamuthu, R.; Subadevi, R.; Sivakumar, M.; Yoo, K.; Kim, J. Eco-friendly production of carbon electrode from biomass for high performance lithium and zinc ion capacitors with hybrid energy storage characteristics. *Mater. Lett.* **2023**, *354*, 135320. [CrossRef]
6. Boruah, B.D.; Mathieson, A.; Wen, B.; Jo, C.; Deschler, F.; Volder, M.D. Photo-rechargeable Zinc-Ion capacitor using 2D graphitic carbon nitride. *Nano Lett.* **2020**, *20*, 5967–5974. [CrossRef]
7. Maughan, P.A.; Tapia-Ruiz, N.; Bimbo, N. In-situ pillared MXene as a viable zinc-ion hybrid capacitor. *Electrochim. Acta* **2020**, *341*, 136061. [CrossRef]
8. Chen, X.; Zhang, H.; Gao, Y.; Liu, J.-H.; Cao, X.; Zhan, C.; Wang, S.; Wang, J.; Dou, S.-X.; Cao, D. Zinc-ion hybrid supercapacitors: Design strategies, challenges, and perspectives. *Carbon Neutralization* **2022**, *1*, 159–188. Available online: https://onlinelibrary.wiley.com/doi/pdfdirect/10.1002/cnl2.22 (accessed on 30 October 2023). [CrossRef]
9. Eskusson, J.; Thomberg, T.; Lust, E.; Jänes, A. Electrochemical characteristics of Zn-ion hybrid supercapacitors based on aqueous solution of different electrolytes. *J. Electrochem. Soc.* **2022**, *169*, 020512. [CrossRef]
10. Wang, Y.; Sun, S.; Wu, X.; Liang, H.; Zhang, W. Status and opportunities of zinc ion hybrid capacitors: Focus on carbon materials, current collectors, and separators. *Nano-Micro Lett.* **2023**, *15*, 78. Available online: https://link.springer.com/content/pdf/10.1007/s40820-023-01065-x.pdf (accessed on 30 October 2023). [CrossRef]
11. Li, Y.; Zhang, X.; Lu, T.; Zhang, Y.; Li, X.; Yu, D.; Zhao, G. Boosting the capacitance of aqueous zinc-ion hybrid capacitors by engineering hierarchical porous carbon architecture. *Batteries* **2023**, *9*, 429. Available online: https://www.mdpi.com/2313-0105/9/8/429/pdf?version=1692264370 (accessed on 30 October 2023). [CrossRef]
12. Tang, H.; Yao, J.; Zhu, Y. Recent developments and future prospects for zinc-ion hybrid capacitors: A review. *Adv. Energy Mater.* **2021**, *11*, 2003994. [CrossRef]
13. Jagadale, A.D.; Rohit, R.C.; Shinde, S.K.; Kim, D. Materials development in hybrid zinc-ion capacitors. *ChemNanoMat* **2021**, *7*, 1082–1098. [CrossRef]
14. Ma, X.; Wang, J.; Wang, X.; Zhao, L.; Xu, C. Aqueous V_2O_5/activated carbon zinc-ion hybrid capacitors with high energy density and excellent cycling stability. *J. Mater. Sci.-Mater. Electron.* **2019**, *30*, 5478–5486. [CrossRef]
15. Pramanik, A.; Chattopadhyay, S.; Maiti, S.; De, G.; Mahanty, S. Hollow-porous nanospheres of $ZnMn_2O_4$ spinel: A high energy density cathode for rechargeable aqueous battery. *Mater. Chem. Phys.* **2021**, *263*, 124373. [CrossRef]
16. Aristote, N.T.; Deng, X.; Zou, K.; Gao, X.; Momen, R.; Li, F.; Deng, W.; Hou, H.; Zou, G.; Ji, X. General overview of sodium, potassium, and zinc-ion capacitors. *J. Alloys Compd.* **2022**, *913*, 165216. [CrossRef]
17. Wang, J.; Wang, J.-G.; Liu, H.; You, Z.; Li, Z.; Kang, F.; Wei, B. A highly flexible and lightweight MnO_2/graphene membrane for superior zinc-ion batteries. *Adv. Funct. Mater.* **2021**, *31*, 2007397. Available online: https://onlinelibrary.wiley.com/doi/pdf/10.1002/adfm.202007397 (accessed on 30 October 2023). [CrossRef]
18. Huang, C.; Wang, Q.; Zhang, D.; Shen, G. Coupling N-doping and rich oxygen vacancies in mesoporous $ZnMn_2O_4$ nanocages toward advanced aqueous zinc ion batteries. *Nano Res.* **2022**, *15*, 8118–8127. [CrossRef]
19. Yang, S.; Zhang, M.; Wu, X.; Wu, X.; Zeng, F.; Li, Y.; Duan, S.; Fan, D.; Yang, Y.; Wu, X. The excellent electrochemical performances of $ZnMn_2O_4/Mn_2O_3$: The composite cathode material for potential aqueous zinc ion batteries. *J. Electroanal. Chem.* **2019**, *832*, 69–74. [CrossRef]
20. Chen, F.; Wang, Q.; Yang, X.; Wang, C.; Zang, H.; Tang, Y.; Li, T.; Geng, B. Construction of hollow mesoporous $ZnMn_2O_4$/C microspheres with carbon nanotubes embedded in shells for high-performance aqueous zinc ions batteries. *Nano Res.* **2023**, *16*, 1726–1732. [CrossRef]
21. Cui, K.; Sun, M.; Zhang, J.; Xu, J.; Zhai, Z.; Gong, T.; Hou, L.; Yuan, C. Facile solid-state synthesis of tetragonal $CuFe_2O_4$ spinels with improved infrared radiation performance. *Ceram. Int.* **2022**, *48*, 10555–10561. [CrossRef]
22. Jiang, H.; Zhang, Y.; Pan, Z.; Xu, L.; Zheng, J.; Gao, Z.; Hu, T.; Meng, C.; Wang, J. Layered $Ca_{0.28}MnO_2{\cdot}0.5H_2O$ as a high performance cathode for aqueous zinc-ion battery. *Small* **2020**, *16*, 2000597. Available online: https://onlinelibrary.wiley.com/doi/pdf/10.1002/smll.202002852 (accessed on 30 October 2023).
23. Gao, F.; Mei, B.; Xu, X.; Ren, J.; Zhao, D.; Zhang, Z.; Wang, Z.; Wu, Y.; Liu, X.; Zhang, Y. Rational design of $ZnMn_2O_4$ nanoparticles on carbon nanotubes for high rate and durable aqueous zinc-ion batteries. *Chem. Eng. J.* **2022**, *448*, 137742. Available online: https://www.sciencedirect.com/science/article/pii/S1385894722032296 (accessed on 30 October 2023). [CrossRef]
24. Gao, Q.; Li, T.; Liu, C.; Sun, J.; Liu, Y.; Hou, L.; Yuan, C. Hierarchically porous N-doped carbon framework with enlarged interlayer spacing as dual-carbon electrodes for potassium ion hybrid capacitors. *Carbon Neutr.* **2023**, *2*, 18. [CrossRef]

25. Tao, Y.; Li, Z.; Tang, L.; Pu, X.; Cao, T.; Cheng, D.; Xu, Q.; Liu, H.; Wang, Y.; Xia, Y. Nickel and cobalt Co-substituted spinel $ZnMn_2O_4$@ N-rGO for increased capacity and stability as a cathode material for rechargeable aqueous zinc-ion battery. *Electrochim. Acta* **2020**, *331*, 135296. [CrossRef]
26. Yang, C.; Han, M.; Yan, H.; Li, F.; Shi, M.; Zhao, L. In-situ probing phase evolution and electrochemical mechanism of $ZnMn_2O_4$ nanoparticles anchored on porous carbon polyhedrons in high-performance aqueous Zn-ion batteries. *J. Power Sources* **2020**, *452*, 227826. [CrossRef]
27. Cai, K.; Luo, S.; Cong, J.; Li, K.; Yan, S.; Hou, P.; Wang, Q.; Zhang, Y.; Liu, X.; Lei, X. Synthesis and optimization of $ZnMn_2O_4$ cathode material for zinc-ion battery by citric acid sol-gel method. *J. Electrochem. Soc.* **2022**, *169*, 030531. [CrossRef]
28. Shi, M.; Wang, B.; Shen, Y.; Jiang, J.; Zhu, W.; Su, Y.; Narayanasamy, M.; Angaiah, S.; Yan, C.; Peng, Q. 3D assembly of MXene-stabilized spinel $ZnMn_2O_4$ for highly durable aqueous zinc-ion batteries. *Chem. Eng. J.* **2020**, *399*, 125627. [CrossRef]
29. Gao, Z.; Lu, G.-G.; Cao, L.-C.; Zhu, Z.-X.; Li, Y.-X.; Wei, F.-X.; Ji, Z.; Sui, Y.-W.; Qi, J.-Q.; Meng, Q.-K.; et al. Rationally designed Mn_2O_3@ $ZnMn_2O_4$/C core–shell hollow microspheres for aqueous zinc-ion batteries. *Dalton Trans.* **2023**, *52*, 1768–1776. Available online: http://pubs.rsc.org/en/content/articlepdf/2023/DT/D2DT03652E (accessed on 30 October 2023). [CrossRef]
30. Mallick, S.; Choutipalli, V.S.K.; Bag, S.; Subramanian, V.; Raj, C.R. Defect engineered ternary spinel: An efficient cathode for an aqueous rechargeable zinc-ion battery of long-term cyclability. *ACS Appl. Mater. Interfaces* **2022**, *14*, 37577–37586. [CrossRef]
31. Deng, S.; Tie, Z.; Yue, F.; Cao, H.; Yao, M.; Niu, Z. Rational design of $ZnMn_2O_4$ quantum dots in a carbon framework for durable aqueous zinc-ion batteries. *Angew. Chem. Int. Ed.* **2022**, *61*, e202115877. [CrossRef]
32. Soundharrajan, V.; Sambandam, B.; Kim, S.; Islam, S.; Jo, J.; Kim, S.; Mathew, V.; Sun, Y.-k.; Kim, J. The dominant role of Mn^{2+} additive on the electrochemical reaction in $ZnMn_2O_4$ cathode for aqueous zinc-ion batteries. *Energy Stor. Mater.* **2020**, *28*, 407–417. [CrossRef]
33. Shao, T.; Zhang, Y.; Cao, T.; Yang, Y.; Li, Z.; Liu, H.; Wang, Y.; Xia, Y. Structural regulation of $ZnMn_2O_4$ cathode material by K, Fe-double doping to improve its rate and cycling stability for rechargeable aqueous zinc-based batteries. *Chem. Eng. J.* **2022**, *431*, 133735. Available online: https://www.sciencedirect.com/science/article/pii/S1385894721053092 (accessed on 30 October 2023). [CrossRef]
34. Cheng, C.; Wu, D.X.; Gong, T.Y.; Yan, Y.S.; Liu, Y.; Ji, X.W.; Hou, L.R.; Yuan, C.Z. Internal and external cultivation design of zero-strain columbite-structured MNb_2O_6 toward lithium-ion capacitors as competitive anodes. *Adv. Energy Mater.* **2023**, *13*, 202302107. [CrossRef]
35. Chen, L.; Yang, Z.; Qin, H.; Zeng, X.; Meng, J. Advanced electrochemical performance of $ZnMn_2O_4$/N-doped graphene hybrid as cathode material for zinc ion battery. *J. Power Sources* **2019**, *425*, 162–169. [CrossRef]